

Characterization of a Novel Binding Protein for Fortilin/TCTP — Component of a Defense Mechanism against Viral Infection in *Penaeus monodon*

Tanate Panrat¹, Patuma Sinthujaroen¹, Benjamas Nupan¹, Warapond Wanna¹, Martti Tapani Tammi^{1,2*}, Amornrat Phongdara^{1*}

1 Center for Genomics and Bioinformatics Research, Faculty of Science, Prince of Songkla University, Songkhla, Thailand, **2** Centre for Research in Biotechnology for Agriculture, Institute of Biological Sciences, University of Malaya, Kuala Lumpur, Malaysia

Abstract

The Fortilin (also known as TCTP) in *Penaeus monodon* (*PmFortilin*) and Fortilin Binding Protein 1 (FBP1) have recently been shown to interact and to offer protection against the widespread White Spot Syndrome Virus infection. However, the mechanism is yet unknown. We investigated this interaction in detail by a number of *in silico* and *in vitro* analyses, including prediction of a binding site between *PmFortilin*/FBP1 and docking simulations. The basis of the modeling analyses was well-conserved *PmFortilin* orthologs, containing a Ca²⁺-binding domain at residues 76–110 representing a section of the helical domain, the translationally controlled tumor protein signature 1 and 2 (TCTP_1, TCTP_2) at residues 45–55 and 123–145, respectively. We found the pairs Cys59 and Cys76 formed a disulfide bond in the C-terminus of FBP1, which is a common structural feature in many exported proteins and the “x–G–K–K” pattern of the amidation site at the end of the C-terminus. This coincided with our previous work, where we found the “x–P–P–x” patterns of an antiviral peptide also to be located in the C-terminus of FBP1. The combined bioinformatics and *in vitro* results indicate that FBP1 is a transmembrane protein and FBP1 interact with N-terminal region of *PmFortilin*.

Citation: Panrat T, Sinthujaroen P, Nupan B, Wanna W, Tammi MT, et al. (2012) Characterization of a Novel Binding Protein for Fortilin/TCTP — Component of a Defense Mechanism against Viral Infection in *Penaeus monodon*. PLoS ONE 7(3): e33291. doi:10.1371/journal.pone.0033291

Editor: Vladimir N. Uversky, University of South Florida College of Medicine, United States of America

Received: September 30, 2011; **Accepted:** February 11, 2012; **Published:** March 12, 2012

Copyright: © 2012 Panrat et al. This is an open-access article distributed under the terms of the Creative Commons Attribution License, which permits unrestricted use, distribution, and reproduction in any medium, provided the original author and source are credited.

Funding: This work was supported by a grant from under The Program Strategic Scholarships for Frontier Research Network for the Ph.D. Program Thai Doctoral degree from the Office of the Higher Education Commission, Thailand (63/2551 to T.P. and 94/2550 to B.N.), The Royal Golden Jubilee Ph.D. Program (PHD/0041/2549 to P.S.), the National Research University of Thailand's Office of the Higher Education Commission of financial support (SCI540527b to W.W.). The funders had no role in study design, data collection and analysis, decision to publish, or preparation of the manuscript.

Competing Interests: The authors have declared that no competing interests exist.

* E-mail: pamornra@yahoo.com (AP); marttit@gmail.com (MTT)

Introduction

The White Spot Syndrome Virus (WSSV) is a common pathogen that causes significant production losses in the shrimp industry around the world. The virus has a wide host range in a variety of crustaceans, both freshwater and seawater species, including *penaeid* shrimp, crabs, and crayfish. A WSSV infection typically causes lethargic behavior, cessation of feeding, a pink to reddish-brown discoloration, and white inclusion of calcium salts embedded in the cuticle especially inside the surface of the carapace. The moribund shrimp swim near the surface at the edge of ponds. The populations of shrimp showing these signs have high mortality rates with cumulative mortalities reaching up to 100% within three to ten days. The transmission of disease is typically via cannibalism of the sick or dying prawns and directly through contaminated water. The virus can persist and retain infectivity in seawater for four to seven days. The histopathology of WSSV infected shrimp shows severe nuclear hypertrophy, chromatin margination, and eosinophilic to large basophilic intranuclear inclusions with variable multifocal necrosis in most tissues of ectodermal and mesodermal origin [1]. The WSSV also severely damages the stomach, gills, antennal gland, heart, and eyes. The infection can be classified into two types: Type I is an acute

infection that causes high mortality within two weeks in species such as *Penaeus monodon*, *Penaeus indicus*, and *Penaeus penicillatus*. Type II is latent.

Based on the morphology and the genomic structures, WSSV has been classified to the genus Whispovirus and the family Nimaviridae. The virions are enveloped, ovoid to bacilliform 276±26 nm long with a diameter of 121±9 nm, containing double-stranded circular DNA with the size ranging from 290 kbp to 305 kbp, which covers approximately 185 open reading frames, ORFs [1–3]. The virion envelope contains two major proteins, VP28 and VP19 of estimated sizes 28 and 19 kDa, respectively. The nucleocapsid consists of three major proteins VP26, VP24 and VP15 of estimated sizes 26, 24, and 15 kDa, respectively [4,5]. A previous study indicates that the gene identified as ORF390 has anti-apoptotic properties, contains two putative caspase9 cleavage sites and a caspase3 cleavage site [6]. The WSSV can replicate and propagate in a number of cell types, such as haematopoietic cell cultures of freshwater crayfish, *Pacifastacus leniusculus* [7], hepatopancreas cells of *Penaeus monodon* [8] and ovarian cultures of *Marsupenaeus japonicas* [9]. The replication rate of the WSSV inside the nucleus of the haematopoietic cell cultures of freshwater crayfish is known to increase with increasing temperature [7].

Over the years, a lot of effort has been put into attempts to protect against WSSV infection in shrimp, such as the usage of random library peptides [10], RNA interference, siRNA, VP15 and VP28 genes and long dsRNA — shown to induce both a sequence-specific and sequence-independent antiviral immunity [11], injection of VP28-dsRNA alone [12], vaccination with viral structural proteins and a monoclonal antibody targeting VP28 [13].

Fortilin (also known as Translationally controlled tumor protein, TCTP) has attracted a lot of attention due to its implication in a variety of functions, i.e., control of cell cycle, cell growth and cell division [14,15], microtubule stabilization [16], and as a growth factor for B-cells [17]. Fortilin is present in both the nucleus and cytosol [18], is inducible by serum stimulation [19] and heavy metals [20]. Fortilin has a potent anti-apoptotic function [18,21–23] through binding interactions with MCL1 (Myeloid cell leukemia 1) [24] and BCL-XL (B-cell leukemia XL) [25], belonging to the anti-apoptosis BCL-2 protein family. Fortilin can also bind to Ca^{2+} [26–29] and thus prevent cytosolic Ca^{2+} levels from increasing and activating Ca^{2+} -dependent apoptosis pathways [28]. Fortilin is thought to be a modulator of GTPase activity, acting as a molecular switch for a vast number of cellular processes in all eukaryotes [30]. Fortilin can bind to Na, K^+ -ATPase and regulates the function of Na, K^+ -ATPase in cooperation with Nexin6 (SNX6) [31]. The Fortilin protein is also known to be involved in growth and development, it is encoded by abundant mRNA species, and was initially characterized in mouse Ehrlich ascites tumor cells and erythroleukemia cells [15,32]. Despite various functions, its wide range of distribution, and high level of conservation among many organisms, the distinct functions of Fortilin still remain unclear [16,20,26–28,33].

Our group has previously identified Fortilin in *Penaeus monodon*, named *Pm*Fortilin (Accession No: AY186580.1) and shown it to have anti-apoptotic properties. This protein is well conserved, contains a Ca^{2+} -binding domain, TCTP signatures similar to that of the Fortilin or TCTP genes reported in plants and animals [29]. We found it to be present at high levels during an onset of viral infection in *P. monodon* and based on a yeast two-hybrid screening assay and GST-pulldown, we further found Fortilin to interact with a previously unknown protein, named Fortilin Binding Protein 1 (FBP1) (Accession No: EU435133.1) [34]. This is a small peptide of 93 amino acids long with a molecular weight of 11 kDa, expressed solely in hemocytes and no homologs have yet been found. It was also of interest that we found transcripts of FBP1 to be up-regulated during WSSV infection with the highest level occurring at 48 h post-infection [34]. In this manuscript we report investigations into the interaction of *Pm*Fortilin with FBP1 and its function. From our results we suggest that FBP1 is a transmembrane protein and its likely function is to facilitate transport of *Pm*Fortilin across the cell membrane.

Results

Structural analysis of *Pm*Fortilin and FBP1

Experimentally determined structures are not available for either *Pm*Fortilin or FBP1. For this reason, we have predicted the structures by homology modeling. The best scoring 3-D structure of *Pm*Fortilin contains three sheets, six beta hairpins, two beta bulges, three helices and one helix-helix interaction. The model displays one helical domain, stretching from residue 77 to 126 and one right handed hook (RHH) of the disulphide type (Figure 1). The model of FBP1 contains two helix domains, 16 beta turns and 12 gamma turns. The two helix domains are located at residues 8

to 21 and residues 23 to 25, forming disulphide bonds between the Cys59 and Cys76 (Figure 2).

To assess the accuracy of the structure predictions, we performed a ramachandran analysis, for *Pm*Fortilin, 108 (72.50%) residues were in the most favored regions, additional allowed regions contained 33 (22.10%) residues, generously allowed regions contained seven (4.70%) residues and disallowed regions contained only a single (0.70%) residue (Figure S1). For the predicted FBP1 structure, 31 (49.20%) residues were plotted in the most favored regions, additional allowed regions contained 21 (33.30%) residues, generously allowed regions contained six (9.50%) residues and five (7.90%) residues were located in the disallowed regions (Figure S2).

*Pm*Fortilin is highly conserved; the chain A has the solution structure of human translationally controlled tumor protein, the chain A with the translationally controlled tumor associated protein p23fyp from *Schizosaccharomyces pombe*, the chains A, B, C, and D with the crystal structure of human translationally controlled tumor associated protein (hTCTP) mutant E12V, the chain A with the crystal structure of translationally controlled tumor associated protein from *Plasmodium knowlesi* and with the Fortilin structure of *Drosophila melanogaster* (PDB ID: 2HR9, 1H6Q, 3EBM, 1TXJ, and 1YZ1 respectively). A further comparison of multiple sequences reveals that *Pm*Fortilin contains conserved regions that correspond to the helical domain in the predicted 3-D structure. The amino acid residues 76–110, part of the helical domain of *Pm*Fortilin are contained within a Ca^{2+} -binding domain, forming a helical domain between the H2-helix (residues 81–99) and the H3-helix (residues 106–122) producing an EF-hand structure (Figure 1). Importantly, a small section at the N-terminus (residues 1–10) contains protein transduction domains (PTDs), 1-MKVFKDMLTG-10, allowing for the delivery of active molecules into the cells through the lipid bilayer [35–37]. *Pm*Fortilin contains two signature patterns. The TCTP_1 and TCTP_2 at the residues 45–55 and 123–145 with the signatures “[FAED]–[GA]–[GASF]–N–[PAK]–S–[GTA]–E–[GDEVCF]–[PAGEQV]–[DEQGAV]” and “[FLIV]–x(4)–[FLVH]–[FY]–[MIVCT]–G–E–x(4,7)–[DENP]–[GAST]–x–[LIVM]–[GAVI]–x(3)–[FYWQ]”, respectively (Table S1).

For FBP1, we were unable to find homologous sequences in the existing public databases. However, we used Motif Scan (http://myhits.isb-sib.ch/cgi-bin/motif_scan) to detect signatures. The search revealed some interesting signatures: Amino acid residues 4–6 at the N-terminal represented by “[ST]–x–[RK]” pattern at protein kinase C phosphorylation site and by “x–G–[RK]–[RK]”, which is a known amidation pattern, were found to be located at the residues 90–93 at the C-terminal end of FBP1 (Table S1). Two segments of compositionally biased regions or Low Complexity Regions (LCRs), were located at the amino acid residues 27–48 and 59–87 using SMART server (<http://smart.embl-heidelberg.de>) (Table S1 and S2), previously implied in the context of protein-protein interactions [38–40]. The residues 1–24 are likely to be a signal peptide (scored 99.00%) with a cleavage site at Ala24 and Thr25 (scored 87.30%), determined by the Signal P 3.0 server (<http://www.cbs.dtu.dk/services/SignalP>). It was of some interest that FBP1 contains a number of “x–P–P–x” signature sequences found in antiviral peptides. The longest such pattern is located at residues 59–76 [34]. In addition, we performed combinatorial structure analyses using GANGSTA and GANGSTA+ servers (<http://agknapp.chemie.fu-berlin.de/gpluss>) (Table S3).

Functional analysis of Fortilin/TCTP binding protein (FBP1)

The predicted 3-D model of FBP1 contains two alpha helix domains. Such segments are common protein structure elements

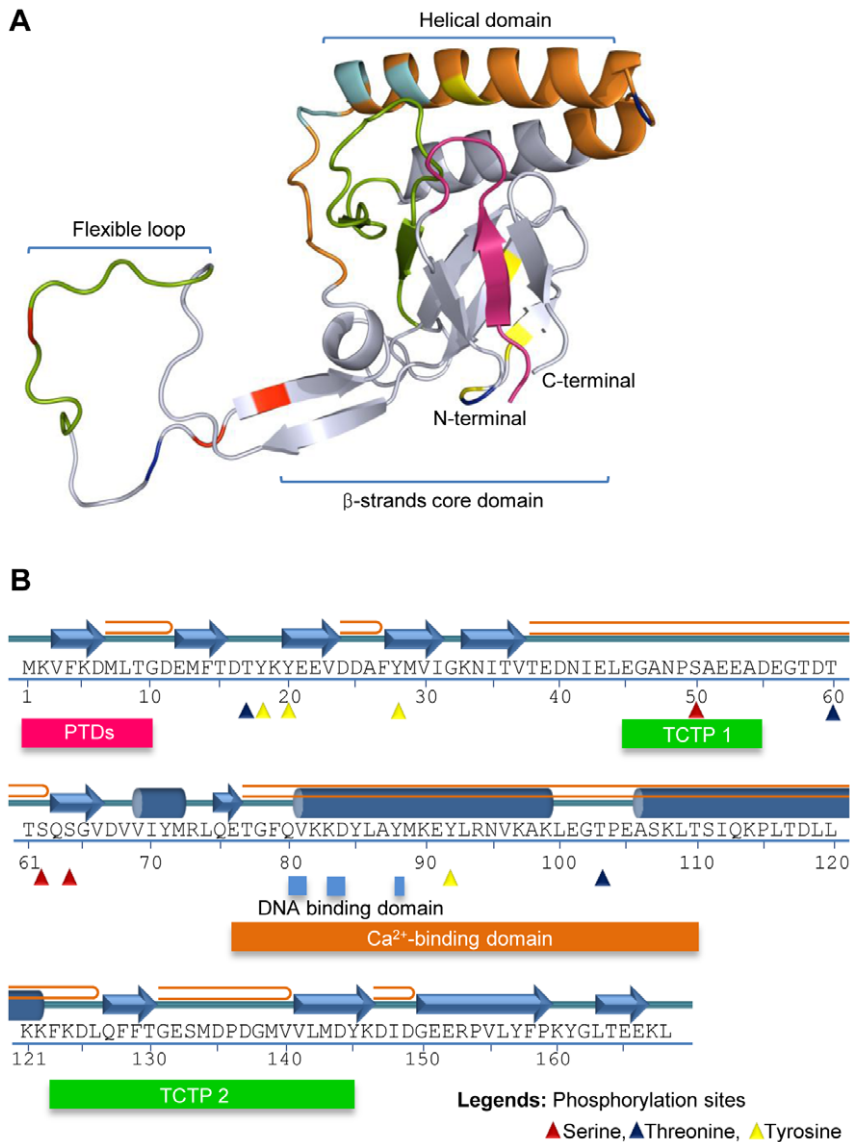


Figure 1. The predicted 3-D model and functional mapping of Fortilin from *Penaeus monodon*. (A) The predicted structure model of *Pm*Fortilin contains six beta hairpins, eleven strands and three helices: The helical domain (helix-helix interaction) along the residues 77–126 and a flexible loop at residues 38–62. (B) A graphical representation of the functional mapping of *Pm*Fortilin protein, was analyzed by SMART and the Motif Scan server. The following elements are shown: TCTP signatures at residues 45–55 on the flexible loop and 123–145 on the C-terminal, Ca²⁺-binding domain at residues 76–110 and DNA binding domain at residues 80–81, 83–84 and 88 also on the helical domains, serine phosphorylation sites at the residues 50, 62 and 64, threonine phosphorylation sites at the residues 17, 60 and 103, tyrosine phosphorylation sites at the residues 18, 20, 28 and 92. The ten amino acid residues at the N-terminal show high conservation with the protein transduction domains (PTDs) and may allow transmembrane transport.

doi:10.1371/journal.pone.0033291.g001

that cross biological membranes. To further assess the topology and possible localization of FBP1, we utilized HMMTOP (<http://www.enzim.hu/hmmtop>) and TMHMM2 servers (<http://www.cbs.dtu.dk/services/TMHMM>). According to these predictions, the helix residues 7–26 are transmembrane segments (Table S1), the residues 1–6 that correspond to the N-terminal phosphorylation site found by Motif Scan are located in the cytosol and the residues 27–93, containing LCRs and “x-P-P-x” signature sequences, are extracellular (Figure 2B).

To find further support to the hypothesis that the FBP1 is a transmembrane protein, we transfected Sf9 cells with a plasmid containing an FBP1-GFP construct. An empty pHMGFP plasmid and mock-transfected cells were used as negative controls.

Confocal laser scanning microscopy was used to observe the fluorescence patterns in the cells 48 h after transfection.

The signals in the Sf9 cells are clearly located at the plasma membrane, whereas the signals in the cells transfected only with GFP are dispersed. The mock-transfected cells show no GFP signal (Figure 3). In addition plasma membranes stained with 1,1'-Diiododecyl-3,3,3',3'-Tetramethylindocarbocyanine Perchlorate (DiI) confirmed the localization of FBP1 (Figure 3, lower panel).

The Co-localization of *Pm*Fortilin and FBP1 by immunocytochemistry

Immunofluorescence studies were performed to investigate the localization of *Pm*Fortilin in the presence of FBP1. A confocal laser

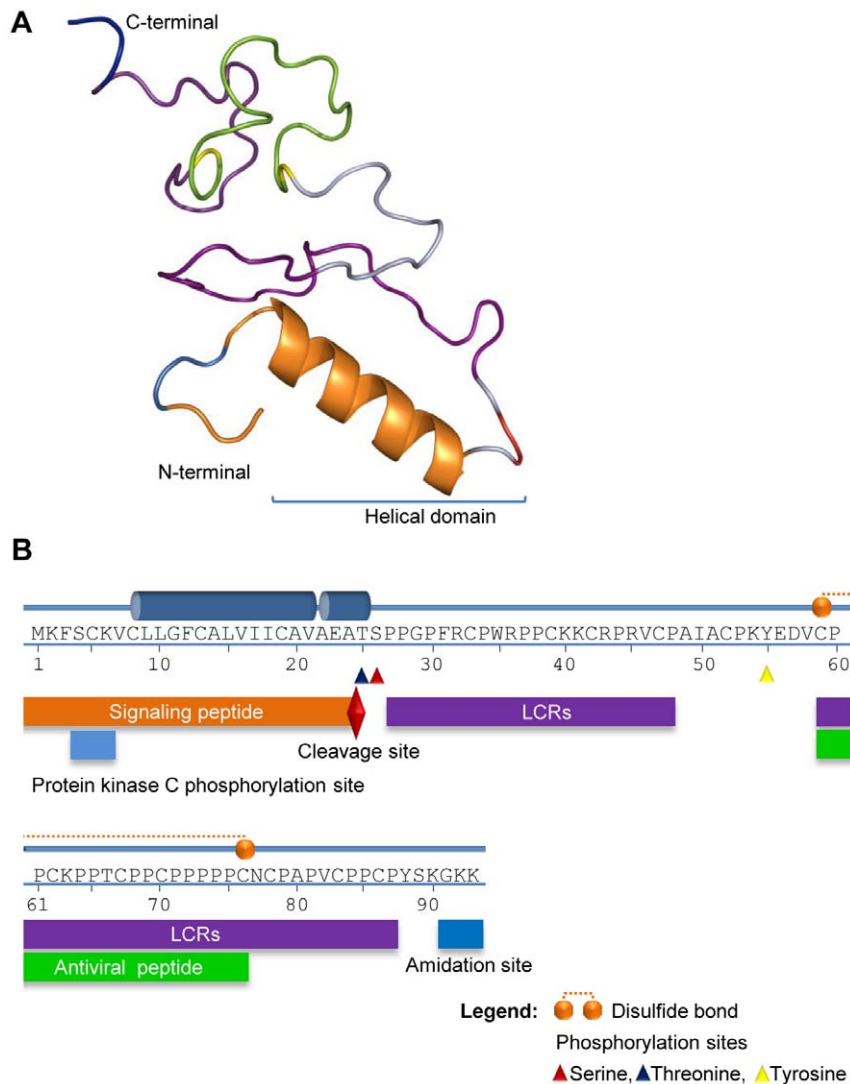


Figure 2. The predicted 3-D model and functional mapping of Fortilin Binding Protein 1. (A) The FBP1 contains two helical domains located at residues 8 to 21 and residues 23 to 25, forming a disulfide bond between the Cys59 and Cys76. (B) A graphical representation of the functional mapping of FBP1. The following elements are shown: Two helix domains, 16 beta turns and 12 gamma turns. A signal peptide at residues 1–24, a cleavage site at residues 22–25, with cleavage between Ala24 and Thr25. A protein kinase C phosphorylation site “[ST]-x-[RK]” at residues 4–6 at the N-terminal. An amidation pattern “x-G-[RK]-[RK]” at residues 90–93 at the C-terminal end. Two segments of compositionally biased regions or Low Complexity Regions (LCRs) at 27–48 and 59–87 and “x-P-P-x” signature sequences of antiviral peptide signatures at 59–76, serine phosphorylation site at the residue 26, threonine phosphorylation site at the residue 25, tyrosine phosphorylation site at the residue 55. doi:10.1371/journal.pone.0033291.g002

scanning microscopy was used to observe the fluorescence patterns in the cells 48 h after transfection. We observed that FBP1-GFP was located at the plasma membrane (Figure 4A) while the staining with the anti-*Pm*Fortilin antibody appeared in the whole cell (Figure 4B). According to previous reports, TCTP/Fortilin was mainly localized in the cytosol and also in the nucleus [14,18]. In this experiment, the co-localization of *Pm*Fortilin and FBP1 was detected as a yellow color only at the plasma membrane (Figure 4C).

*Pm*Fortilin/FBP1 docking simulations and interaction analysis

To further analyze the *Pm*Fortilin and FBP1 interaction in detail, we predicted the *Pm*Fortilin/FBP1 binding site residues and performed docking simulations utilizing the ClusPro 2.0 server (<http://cluspro.bu.edu>), including the PIPER docking software based on the Fast Fourier Transform (FTT) method [41], using

FBP1 as a receptor protein and *Pm*Fortilin as a ligand. The models were predicted using four separate modes: Balance, Electrostatic, Hydrophobic and VdW+Elec mode. The short interacting elements were extracted from the best scoring interaction complex and collected to produce a refined model (Figure 5). The best, i.e. the lowest docking score of the balance mode is -993.40 Kcal/mol and highest -764.20 Kcal/mol. The average score of the docking energy center is -811.29 Kcal/mol and the lowest docking energy score is -871.40 Kcal/mol (Table S4). The electrostatic mode: Lowest docking score is $-1,262.30$ Kcal/mol and highest -990.60 Kcal/mol, the average of the docking energy center is $-1,034.04$ Kcal/mol and lowest docking energy score is $-1,117.93$ Kcal/mol (Table S5), the hydrophobic mode: Lowest docking score is $-1,230.50$ Kcal/mol and highest -951.50 Kcal/mol, the average docking energy center is -940.41 Kcal/mol and the lowest docking energy score is $-1,045.73$ Kcal/mol (Table S6)

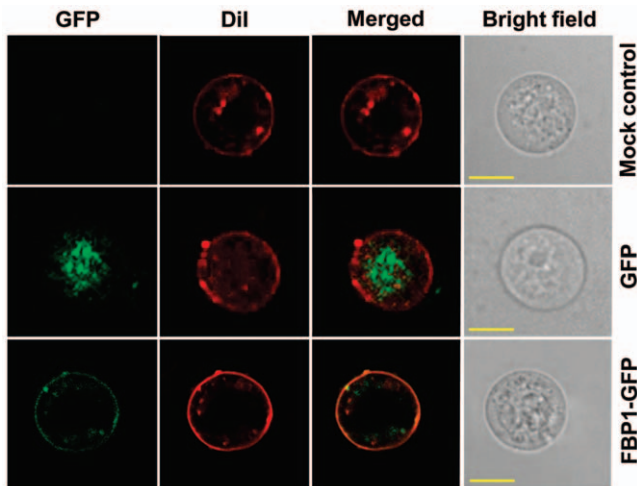


Figure 3. Transmembrane localization of FBP1-GFP in Sf9 cell. The cellular localization of FBP1-GFP expressed in Sf9 cell was observed using confocal laser scanning microscopy at 48 h post-transfection. The plasma membrane was stained with Dil (Invitrogen) and shows co-localization of both fluorescent (green for GFP and red for Dil) after merging. Bright field is shown in the last panel. The scale bars indicate 10 μ m. doi:10.1371/journal.pone.0033291.g003

and the VdW+Elec mode: The lowest docking score is -387.90 Kcal/mol and highest -315.70 Kcal/mol, the average of docking energy center is -315.00 Kcal/mol and the lowest docking energy score obtained is -340.49 Kcal/mol (Table S7).

According to the docking simulations, the flexible region of *Pm*Fortilin binds to the C-terminus of FBP1. These interactions are represented in two major conformations A and B (Figure 5A). The

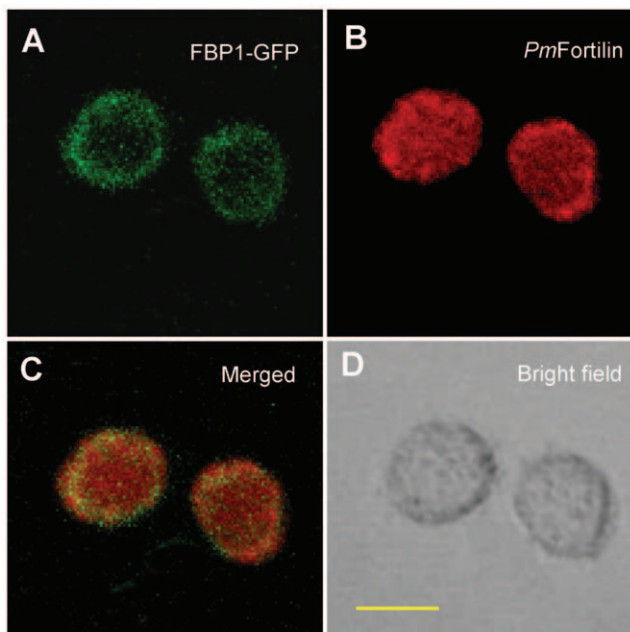


Figure 4. Live-cell and confocal imaging of the subcellular co-localization of GFP-FBP1 and *Pm*Fortilin. After co-transfection (48 h), the sf9 cells were fixed with paraformaldehyde and stained with rabbit anti-*Pm*Fortilin antibody, followed by Alexa Fluor 647-conjugated goat anti-rabbit IgG antibody (Invitrogen). The cells were observed with a confocal laser scanning microscope. The scale bars indicate 10 μ m. doi:10.1371/journal.pone.0033291.g004

balance mode simulation resulted in 25 separate models. The conformation A is favored over conformation B with frequencies 18/25 (72.00%) and 7/25 (28.00%) respectively (Figure 5B). Four of the top five ranking conformations are described in Table S4. The electrostatic mode yields the frequencies 17/23 (73.91%) and 6/23 (26.09%) for the conformations A and B respectively (Figure 5C), the hydrophobic mode yields the frequency 6/23 (26.09%) for conformation A and 17/23 (73.91%) for conformation B (Figure 5D) and the VdW+Elec mode yields the frequencies 22/23 (95.65%) and 1/23 (4.35%) for conformations A and B, respectively (Figure 5E). The frequencies seem to be in good agreement, except for the hydrophobic mode, where the conformation B is the most favored.

These interactions coincide with three domains: (1) the TCTP_1 on the flexible loop of *Pm*Fortilin (Figure 6A-left; green color) with the distance scores of 5.02 and 5.57 respectively for (*Pm*Fortilin_Alal47)-(FBP1_Try88; FBP1_Asn77), 5.26 and 5.60 for (*Pm*Fortilin_Asn48)-(FBP1_Asn77; FBP1_Cys78) and 5.51 for the interaction of (*Pm*Fortilin_Ala51)-(FBP1_Pro79). (2) The predicted Ca²⁺-binding domain (Figure 6A-left; orange color) with the distance score of 4.80 for (*Pm*Fortilin_Thr77)-(FBP1_Pro48), 4.72 and 4.70 for (*Pm*Fortilin_Gly78)-(FBP1_Pro48; FBP1_Ala49). (3) The TCTP_2 on the C-terminal of *Pm*Fortilin (Figure 6A-left; light blue color) with the distance scores of 12.31 for (*Pm*Fortilin_Gln127)-(FBP1_Ala51), 9.96 for (*Pm*Fortilin_Phe128)-(FBP1_Pro48), 9.74 for (*Pm*Fortilin_Phe129)-(FBP1_Pro48), and 11.59 for (*Pm*Fortilin_Met134)-(FBP1_Pro44), according to the balance mode (Figure 6B-D).

The docking simulations predict two distinct conformations. This implies a trimer: FBP1-*Pm*Fortilin-FBP1. For this reason, we performed additional docking simulations, this time simultaneously using two FBPs as receptors. In the trimer structure, the Ca²⁺-binding domains and the flexible loop of the *Pm*Fortilin structure interacted as in the dimer (FBP1-*Pm*Fortilin) simulations. The trimer docking simulation based on the balance mode gave the lowest docking energy score of $-1,162.00$ Kcal/mol and the highest -888.70 Kcal/mol, the average of docking energy being -986.43 Kcal/mol (Figure 7 and Figure S3A-D).

Yeast two-hybrid assay – N-terminal region of *Pm*Fortilin is responsible for interaction with FBP1

According to the docking simulations, the *Pm*Fortilin binds FBP1 at residues 37–63 located on the flexible loop of the *Pm*Fortilin N-terminus and contacts FBP1 at residues 77–88. To confirm the docking results, we sub-cloned *Pm*Fortilin in three separate fragments: *Pm*FT1 (residues 1–70), *Pm*FT2 (residues 71–120) and *Pm*FT3 (residues 121–168). The interaction of FBP1 with each of the three fragments was tested by the yeast two-hybrid assay. The yeast growth in YPDA was monitored to ensure that there were no growth defects in all recombinant clones (Figure 8A). After co-transformation, the clones that harbored the binding proteins were selected from a selective medium, at this step there were no clones found from the yeast harboring BD-*Pm*FT2+ AD-FBP1 (Table 1). This indicated that these two proteins did not interact with each other. The β -galactosidase filter assay was then used to test the yeast harboring BD-*Pm*FT1+AD-FBP1 and that harboring BD-*Pm*FT3+AD-FBP1. The result confirmed an interaction only for BD-*Pm*FT1+AD-FBP1, thereby supporting the docking results (Figure 8B). Further investigations are required to understand the binding of *Pm*Fortilin and FBP1.

Discussion

In previous report FBP1 was identified and cloned from the library by yeast two hybrid screening using *Pm*Fortilin as the bait.

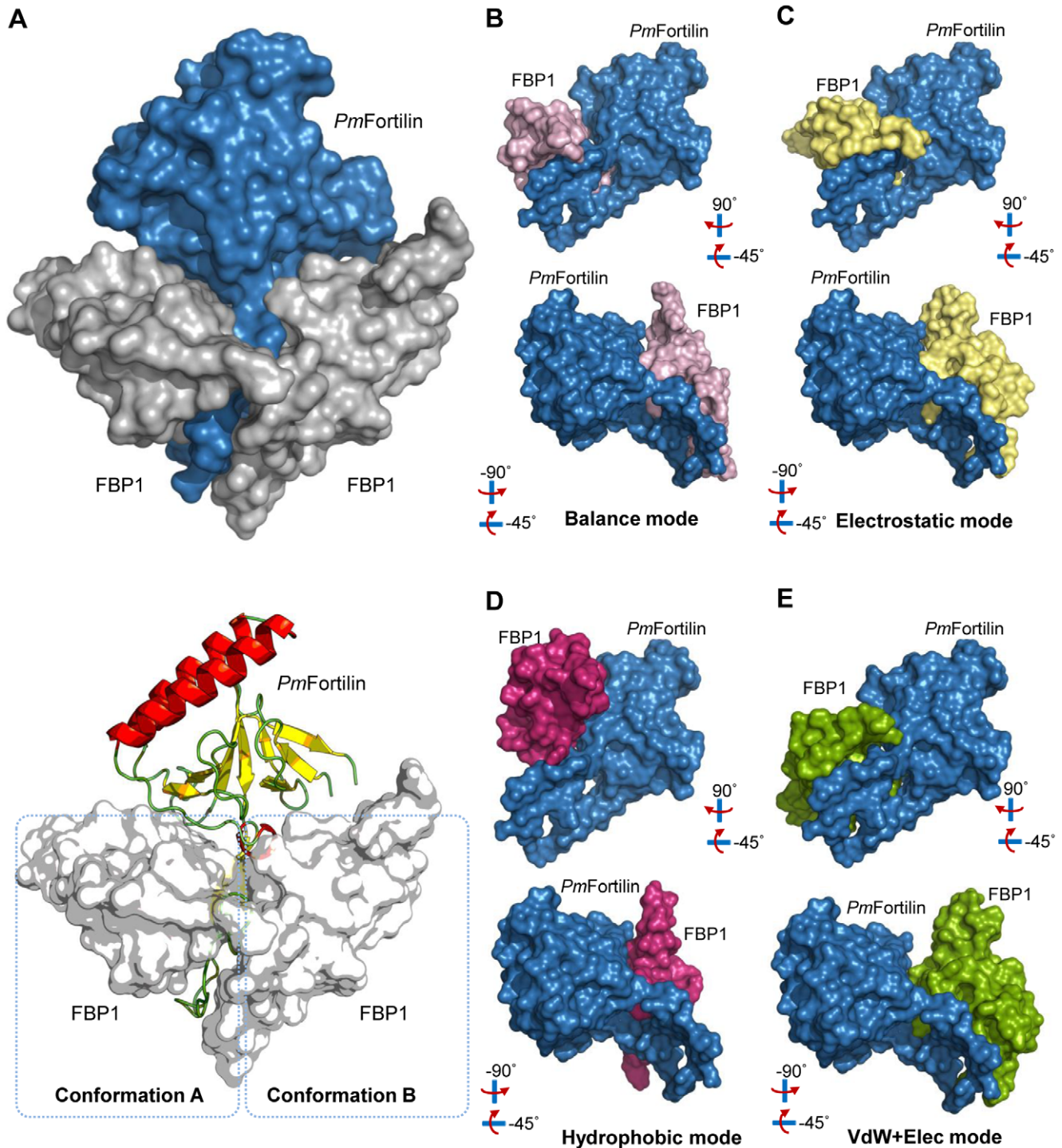


Figure 5. Molecular interaction models of *PmFortilin*/FBP1. (A top) A space-filling model representing the combination of two possible interactions of FBP1 (grey), at the opposite sides of *PmFortilin* (blue). (A bottom) A cartoon of the space-filling model showing the two conformations, A and B and the binding of *PmFortilin* to the C-terminus of FBP1. The predictions were performed with four separate modes: Balance, Electrostatic, Hydrophobic and VdW+Elec mode. (B–E) The lowest energy conformations of each of the four docking modes. The *PmFortilin* molecule (blue) and FBP1 (pink, yellow, magenta and green).
doi:10.1371/journal.pone.0033291.g005

The interaction of these two proteins was confirmed by GST pull down [34]. Both *PmFortilin* and FBP1 transcripts have been shown to be up regulated during a viral infection, thus implying a role in a defense mechanism against viruses. Here we try to accelerate a way to design proper biochemical experiments for the functional

analysis of a novel gene product, FBP1 by using *in silico* methods. We have identified FBP1 as a membrane binding protein and analyzed its interaction with *PmFortilin*. The prediction was supported by the co-localization of Fortilin and FBP1 at the same position on plasma membrane. The contact sites of *PmFortilin* are

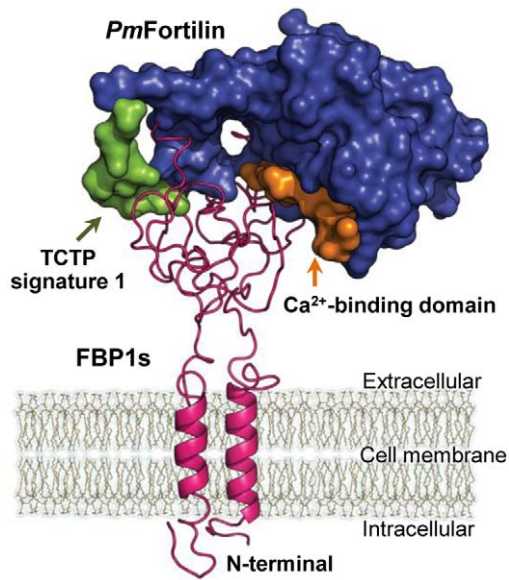


Figure 7. The *Pm*Fortilin/FBP1 trimer (FBP1-*Pm*Fortilin-FBP1) interaction complex. The Ca²⁺-binding domain (orange) and the TCTP_1 of the flexible loop (green). The trimer docking simulation based on the balance mode yielded the lowest docking energy score of $-1,162.00$ Kcal/mol, the highest -888.70 Kcal/mol and the average docking energy of -986.43 Kcal/mol.
doi:10.1371/journal.pone.0033291.g007

the cell membrane. Additional docking simulations further indicate that *Pm*Fortilin can bind two FBP1s simultaneously and thus may be active as a trimer. However, further investigations are needed to decipher the detailed mechanism of transport, phosphorylation and cleavage.

Materials and Methods

Molecular modeling

The homology modeling for the 2-D and 3-D structures were performed with SWISS-MODEL [42] and I-TASSER [43]. The best template was automatically selected based on multiple-threading simulations and used for the structural model. Each of

Table 1. Summary of the growth of yeast harboring recombinant plasmids.

Yeast harboring plasmids	YPDA	Selective medium
BD-FT1 + AD-FBP1	++++	++++
BD-FT2 + AD-FBP1	++++	–
BD-FT3 + AD-FBP1	++++	+++

+, the growth was observed within 3 days; –, no growth.
doi:10.1371/journal.pone.0033291.t001

the predicted models was validated based on the best scoring model given by the PROCHECK software [44]. These were evaluated by ramachandran plot analysis utilizing ProFunc [45] (<http://www.ebi.ac.uk/thornton-srv/databases/profunc>) and PROCHECK software. The 3-D template structures were brought from the PDB database (<http://swissmodel.expasy.org>).

Functional and molecular homology analysis

The GANGSTA and GANGSTA+ [46] were used for comparisons of the 3-D structures of *Pm*Fortilin and FBP1. Motif Scan [47] and SMART [48] were used for scanning signature domains of the *Pm*Fortilin and FBP1 with the default parameters, including outlier homologs and homologs of known structures, Pfam domains, signal peptides, internal repeats and intrinsic protein disorder databases.

The ProFunc server was used to identify the potential functions within the 3-D structures. The HMMTOP [49] with the ‘reliable’ mode and Baum-Welch iteration and TMHMM servers [50] were utilized to predict helical transmembrane segments and the topology with default parameters. Signal peptides and cleavage site patterns were predicted using the SignalP server [51], trained on eukaryotes. Multiple sequence alignments were constructed by using Clustal [52].

Molecular docking simulations and analysis of the interaction model

The molecular interaction and docking simulations were performed using the ClusPro 2.0 server [53]. The interaction

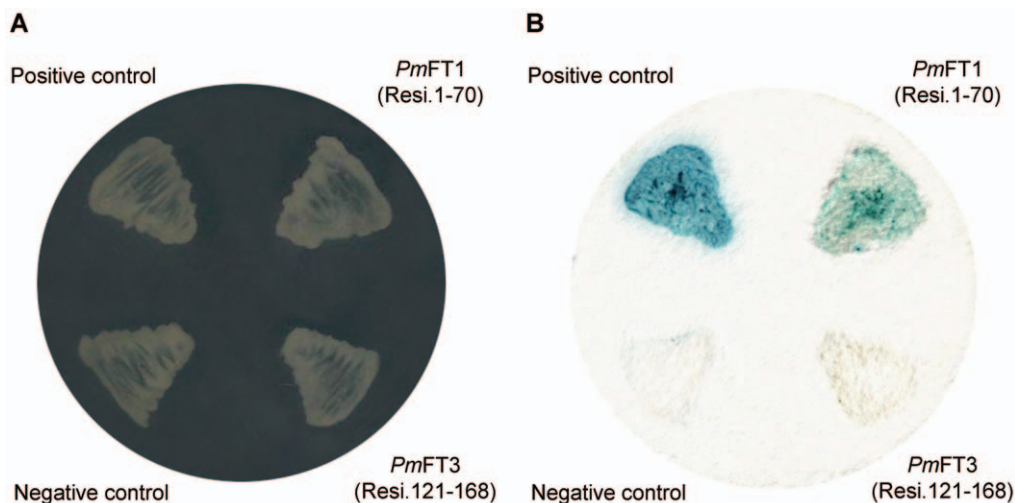


Figure 8. The yeast two-hybrid assay. The yeast two-hybrid interaction between *Pm*Fortilin fragments and FBP1 in *S.cerevisiae* AH109 cells. (A) YPD control to show yeast growth. (B) β -galactosidase activity of the yeast cultures in selective medium determined by a colony-lift filter assay.
doi:10.1371/journal.pone.0033291.g008

elements, such as the residue members, clusters and docking energy values were extracted and collected for simulation. The model of the interaction complex was assessed by the root mean square deviation (RMSD) value and the top ranking, i.e. the lowest docking energy score was used to build the construct of the interaction model. The molecular surfaces and protein structure models in the figures are built and visualized with the PyMOL [54] software on the BioSLAX suite (<http://www.bioslax.com>).

Construction of recombinant FBP1-GFP and confocal microscopy

FBP1 was cloned into the pHMGFP vector (Promega, catalogue no. E6421) to generate an FBP1-GFP fusion protein. PCR was performed with forward primer FBP1-F: 5'-GCTAGCAT-GAAGTTCTCATGT; containing *NheI* site and reverse primer FBP1-R: 5'-CCCGGGCTTCTTGCCCTTACT; containing the *XmaI* site without the stop codon at its C-terminal. The fragments were blunt-end inserted into pHMGFP amplified by transformation into the high efficiency *Escherichia coli* Top10F³ competent (Invitrogen) by the heat shock method. The plasmids were extracted and purified with QIAprep Spin Miniprep Kit (Qiagen). The Sf9 cells were seeded at a density of 5×10^5 cells onto the cover slips in Sf9-S2 medium (PPA). The pHMGFP and pHMGFP-FBP1 plasmids were transfected into Sf9 cells using TransfastTM Transfection reagent (Invitrogen) according to the product instructions and cultured in a 28°C incubator. After 48 h of transfection, the cells were washed by PBS twice. The plasma membrane was stained with 2 mM DiI (Invitrogen) for 15 min at 4°C and the Sf9 cells were observed directly with the confocal laser scanning microscope.

Localization of *Pm*Fortilin in the presence of FBP1 by immunocytochemist

Sf9 cells, at a density of 5×10^6 cells, were grown on glass coverslips in Sf9-S2 medium (PPA), then cotransfected with pHMGFP-FBP1 and pCDNA-*Pm*Fortilin using TransfastTM Transfection reagent (Invitrogen) according to the product instructions. Cells were cultured in a 28°C incubator. 48 h post-transfection, the cells were washed twice with phosphate-buffered saline (PBS) and fixed with 4% paraformaldehyde for 10 min followed by washing with 0.1% Triton x-100 in PBS for 3 min at 4°C. Fixed cells were washed again with PBS before blocking with 5% skim milk at 4°C for 1 h. After incubating, cells were washed and incubated with specific rabbit anti-*Pm*Fortilin antibody (dilution of 1:500 in PBS) at 4°C for 16–18 h. The cells were washed 3 times with PBST and incubated with Alexa flour 647-conjugated goat anti-rabbit IgG antibody (Invitrogen, 1:1,000 in PBS) at room temperature for 2 h. After washing 3 times with PBST, the cover glasses were mounted with 10% glycerol in PBS. The fluorescence signal was detected using a confocal laser scanning microscope (Olympus FV300).

Yeast two-hybrid assay

The yeast two-hybrid screens were performed with the Clontech Matchmaker GAL4 Two-Hybrid System 3 (Clontech Laboratories, Inc., Mountain View, CA, USA). *Pm*Fortilin was divided into 3 fragments: *Pm*FT1 (residues 1–70), *Pm*FT2 (residues 71–120) and *Pm*FT3 (residues 121–168). Plasmids pGBKT7 (named BD vectors) were used for construction of BD-*Pm*Fortilin. The plasmids were constructed by inserting into *EcoRI* and *SalI* sites on a BD-bait vector. Each fragment was amplified by PCR using the following primers;

BD-*Pm*FT1:

BD-*Pm*FT1-F: 5'-CGGAATTCATGAAGGTCCTTCAAG,

BD-*Pm*FT1-R: 5'-GCGTCGACTCATATAACTACATCAACAC

BD-*Pm*FT2:

BD-*Pm*FT2-F: 5'-GGAATTCATATATGCGTCTGCAGGAAAC,

BD-*Pm*FT2-R: 5'-GCGTCGACTCACAAAAGGTCCTGTCA

and BD-*Pm*FT3:

BD-*Pm*FT3-F: 5'-CGGAATTC AAGAAGTTCAAG-GACTTGCA,

BD-*Pm*FT3-R: 5'-GCGTCGACTTATAGCTTCTCCTCTGT.

The plasmid pGADT7 (named AD vector) was used for construction of the AD-FBP1 and contained the *BamHI* and *XhoI* sites;

AD-FBP1:

AD-FBP1-F: 5'-GGATCCCGATGAAGTTCTCATG-TAAAGT,

AD-FBP1-R: 5'-CCCTCGAGTTACTTCTTGCCCTTAC-TAT.

All plasmids constructed were verified by sequencing. Competent yeast cells, *Saccharomyces cerevisiae* strain AH109 were co-transformed either with BD-*Pm*FT1 and AD-FBP1, BD-*Pm*FT2 and AD-FBP1, BD-*Pm*FT3 and AD-FBP1. Cells were then spread on SD selective medium lacking tryptophan, leucine, histidine and adenine (SD-TLHA). The plates were incubated at 30°C until positive colonies were visible after 2–4 days. The transformations were confirmed by PCR. The positive clones were in addition assayed by a filter lift β -galactosidase assay for LacZ activity as described in the manufacturer's protocols.

Supporting Information

Figure S1 The ramachandran analysis of the Fortilin model from *Penaeus monodon*. The number of residues in most favored regions [A, B, L] is 108 (72.50%), the number of residues in additional allowed regions [a, b, l, p] is 33 (22.10%), the number of residues in generously allowed regions [\sim a, \sim b, \sim l, \sim p] is 7 (4.70%) and one (0.70%) residue in disallowed regions. The number of non-glycine and non-proline residues is 149 (88.69%), the number of end-residues (excl. Gly and Pro) is 2 (1.19%), the number of glycine residues (shown as triangles) is 11 (6.55%) and the number of proline residues is 6 (3.57%). (TIF)

Figure S2 The ramachandran analysis of the FBP1 model. The number of residues in most favoured regions [A, B, L] is 31 (49.20%), the number of residues in additional allowed regions [a, b, l, p] is 21 (33.30%), the number of residues in generously allowed regions [\sim a, \sim b, \sim l, \sim p] is 6 (9.50%), the number of residues in disallowed regions is 5 (7.90%). The number of non-glycine and non-proline residues is 63 (67.74%), the number of end-residues (excl. Gly and Pro) is 2 (2.15%), the number of glycine residues (shown as triangles) is 3 (3.23%) and the number of proline residues is 25 (26.88%). (TIF)

Figure S3 Multimer simulations of *Pm*Fortilin/FBP1 interaction model, based on balance mode, FBP1 as the receptor and

*Pm*Fortilin as the ligand. (A) The simulation results of the FBP1 monomer combined with two *Pm*Fortilin molecules (1:2), yields the lowest docking energy of -913.00 Kcal/mol. (B) FBP1 monomer combined with three *Pm*Fortilins (1:3), yields the lowest docking energy of $-1,244.80$ Kcal/mol. (C) Two FBP1 molecules combined with two *Pm*Fortilins (2:2), yields the lowest docking energy of $-1,015.80$ Kcal/mol. (D) Two FBP1 molecules and three *Pm*Fortilins (2:3), yields the lowest docking energy of $-1,015.80$ Kcal/mol. The Ca^{2+} -binding domain orange color and the TCTP signature 1 of the flexible loop is green.

(TIF)

Table S1 The SMART and Motif Scan analysis for *Pm*Fortilin and FBP1. (DOCX)

Table S2 The SMART analysis result of FBP1 on the SMART database. (DOCX)

Table S3 The 3D structure alignment of FBP1 on ASTRAL40 database (version 1.75). (DOCX)

References

- Jory DE, Dixon HM (1999) Shrimp white spot virus in the western hemisphere. *Aquac Mag* 25: 83–91.
- Sangamaheswaran AP, Jeyaseelan MJP (2001) White spot viral disease in penaeid shrimp- A review. *Naga, The ICLARM Quarterly* 24: 16–22.
- van Hulst MC, Witteveldt J, Peters S, Kloosterboer N, Tarchini R, et al. (2001) The white spot syndrome virus DNA genome sequence. *Virology* 286: 7–22.
- van Hulst MC, Goldbach RW, Vlaskovska J (2000) Three functionally diverged major structural proteins of white spot syndrome virus evolved by gene duplication. *J Gen Virol* 81: 2525–2529.
- van Hulst MC, Reijnders M, Vermeesch AM, Zandbergen F, Vlaskovska J (2002) Identification of VP19 and VP15 of white spot syndrome virus (WSSV) and glycosylation status of the WSSV major structural proteins. *J Gen Virol* 83: 257–265.
- Wang Z, Hu L, Yi G, Xu H, Qi Y, et al. (2004) ORF390 of white spot syndrome virus genome is identified as a novel anti-apoptosis gene. *Biochem Biophys Res Commun* 325: 899–907.
- Jiravanichpaisal P, Sricharoen S, Soderhall I, Soderhall K (2006) White spot syndrome virus (WSSV) interaction with crayfish haemocytes. *Fish Shellfish Immunol* 20: 718–727.
- Uma A, Prabhakar TG, Koteswaran A, Ravikumar G (2002) Establishment of primary cell culture from hepatopancreas of *Penaeus monodon* for the study of white spot syndrome virus (WSSV). *Asian Fish Sci* 15: 365–370.
- Maeda M, Saitoh H, Mizuki E, Itami T, Ohba M (2004) Replication of white spot syndrome virus in ovarian primary cultures from the kuruma shrimp, *Marsupenaeus japonicus*. *J Virol Methods* 116: 89–94.
- Yi G, Qian J, Wang Z, Qi Y (2003) A phage-displayed peptide can inhibit infection by white spot syndrome virus of shrimp. *J Gen Virol* 84: 2545–2553.
- Westenberg M, Heinhuis B, Zuidema D, Vlaskovska J (2005) siRNA injection induces sequence-independent protection in *Penaeus monodon* against white spot syndrome virus. *Virus Res* 114: 133–139.
- Sarathi M, Simon MC, Ahmed VPI, Kumar SR, Hameed AS (2008) Silencing VP28 gene of white spot syndrome virus of shrimp by bacterially expressed dsRNA. *Mar Biotechnol* 10: 198–206.
- Witteveldt J, Cifuentes CC, Vlaskovska J, van Hulst MC (2004) Protection of *Penaeus monodon* against white spot syndrome virus by oral vaccination. *J Virol* 78: 2057–2061.
- Bommer UA, Thiele BJ (2004) The translationally controlled tumour protein (TCTP). *Int J Biochem Cell Biol* 36: 379–385.
- Gachet Y, Tournier S, Lee M, Lazaris-Karatzas A, Poulton T, et al. (1999) The growth-related, translationally controlled protein P23 has properties of a tubulin binding protein and associates transiently with microtubules during the cell cycle. *J Cell Sci* 112: 1257–1271.
- Yarm FR (2002) Plk phosphorylation regulates the microtubule-stabilizing protein TCTP. *Mol Cell Biol* 22: 6209–6221.
- Kang HS, Lee MJ, Song H, Han SH, Kim YM, et al. (2001) Molecular identification of IgE-dependent histamine-releasing factor as a B cell growth factor. *J Immunol* 166: 6545–6554.
- Li F, Zhang D, Fujise K (2001) Characterization of fortilin, a novel antiapoptotic protein. *J Biol Chem* 276: 47542–47549.
- Benndorf R, Nurnberg P, Bielka H (1988) Growth phase-dependent proteins of the Ehrlich ascites tumor analyzed by one- and two-dimensional electrophoresis. *Exp Cell Res* 174(1): 130–138.
- Sturzenbaum SR, Kille P, Morgan AJ (1998) Identification of heavy metal induced changes in the expression patterns of the translationally controlled tumour protein (TCTP) in the earthworm *Lumbricus rubellus*. *Biochim Biophys Acta* 1398: 294–304.
- Graidist P, Phongdara A, Fujise K (2004) Antiapoptotic protein partners fortilin and MCL1 independently protect cells from 5-fluorouracil-induced cytotoxicity. *J Biol Chem* 279: 40868–40875.
- Graidist P, Fujise K, Wanna W, Sritunyalucksana K, Phongdara A (2006) Establishing a role for shrimp fortilin in preventing cell death. *Aquaculture* 255: 157–164.
- Graidist P, Yazawa M, Tonganunt M, Nakatomi A, Lin CC, et al. (2007) Fortilin binds Ca^{2+} and blocks Ca^{2+} -dependent apoptosis *in vivo*. *Biochem J* 408: 181–191.
- Zhang D, Li F, Weidner D, Mnjoyan ZH, Fujise K (2002) Physical and functional interaction between myeloid cell leukemia 1 protein (MCL1) and Fortilin. The potential role of MCL1 as a fortilin chaperone. *J Biol Chem* 277: 37430–37438.
- Yang Y, Yang F, Xiong Z, Yan Y, Wang X, et al. (2005) An N-terminal region of translationally controlled tumor protein is required for its antiapoptotic activity. *Oncogene* 24: 4778–4788.
- Kim M, Jung Y, Lee K, Kim C (2000) Identification of the calcium binding sites in translationally controlled tumor protein. *Arch Pharm Res* 23: 633–636.
- Sanchez JC, Schaller D, Ravier F, Golaz O, Jaccoud S, et al. (1997) Translationally controlled tumor protein: a protein identified in several nontumoral cells including erythrocytes. *Electrophoresis* 18: 150–155.
- Xu A, Bellamy AR, Taylor JA (1999) Expression of translationally controlled tumour protein is regulated by calcium at both the transcriptional and post-transcriptional level. *Biochem J* 342: 683–689.
- Bangrak P, Graidist P, Chotigeat W, Phongdara A (2004) Molecular cloning and expression of a mammalian homologue of a translationally controlled tumor protein (TCTP) gene from *Penaeus monodon* shrimp. *J Biotechnol* 108: 219–226.
- Vernoud V, Horton AC, Yang Z, Nielsen E (2003) Analysis of the small GTPase gene superfamily of Arabidopsis. *Plant Physiol* 131: 1191–1208.
- Jung J, Kim M, Kim MJ, Kim J, Moon J, et al. (2004) Translationally controlled tumor protein interacts with the third cytoplasmic domain of Na, K⁺ATPase alpha subunit and inhibits the pump activity in HeLa cells. *J Biol Chem* 279: 49868–49875.
- Yenofsky R, Cereghini S, Krowczynska A, Brawerman G (1983) Regulation of mRNA utilization in mouse erythroleukemia cells induced to differentiate by exposure to dimethyl sulfoxide. *Mol Cell Biol* 3: 1197–1203.
- van de Sande WW, Janse DJ, Hira V, Goedhart H, van der Zee R, et al. (2006) Translationally controlled tumor protein from *Madurella mycetomatis*, a marker for tumorous mycetoma progression. *J Immunol* 177: 1997–2005.
- Tonganunt M, Nupan B, Saengsakda M, Suklour S, Wanna W, et al. (2008) The role of Pm-fortilin in protecting shrimp from white spot syndrome virus (WSSV) infection. *Fish Shellfish Immunol* 25: 633–637.

Table S4 List of the balance mode docking simulation of *Pm*Fortilin/FBP1. (DOCX)

Table S5 List of the electrostatic mode docking simulation of *Pm*Fortilin/FBP1. (DOCX)

Table S6 List of the hydrophobic mode docking simulation of *Pm*Fortilin/FBP1. (DOCX)

Table S7 List of the VdW+Elec mode docking simulation of *Pm*Fortilin/FBP1. (DOCX)

Acknowledgments

We are grateful to the Office of the Higher Education Commission, Thailand, the Royal Golden Jubilee Ph.D. Program, the Graduated School and the Faculty of Science, Prince of Songkla University.

Author Contributions

Conceived and designed the experiments: TP PS WW MTT AP. Performed the experiments: TP PS BN. Analyzed the data: TP PS BN WW MTT. Contributed reagents/materials/analysis tools: MTT AP. Wrote the paper: TP PS MTT AP.

35. Kim M, Kim M, Kim HY, Kim S, Jung J, et al. (2011) A protein transduction domain located at the NH₂-terminus of human translationally controlled tumor protein for delivery of active molecules to cells. *Biomaterials* 32: 222–230.
36. Schwarze SR, Hruska KA, Dowdy SF (2000) Protein transduction: unrestricted delivery into all cells? *Trends Cell Biol* 10: 290–295.
37. Kim M, Maeng J, Jung J, Kim HY, Kim HJ, et al. (2011) Design and evaluation of variants of the protein transduction domain originated from translationally controlled tumor protein. *Eur J Pharm Sci* 43: 25–31.
38. Coletta A, Pinney JW, Solis DY, Marsh J, Pettifer SR, et al. (2010) Low-complexity regions within protein sequences have position-dependent roles. *BMC Syst Biol* 4: 43.
39. DePristo MA, Zilversmit MM, Hartl DL (2006) On the abundance, amino acid composition, and evolutionary dynamics of low-complexity regions in proteins. *Gene* 378: 19–30.
40. Wootton JC, Federhen S (1993) Statistics of local complexity in amino acid sequences and sequence databases. *Comput Chem* 17: 149–163.
41. Kozakov D, Brenke R, Comeau SR, Vajda S (2006) PIPER: an FFT-based protein docking program with pairwise potentials. *Proteins* 65: 392–406.
42. Arnold K, Bordoli L, Kopp J, Schwede T (2006) The SWISS-MODEL workspace: a web-based environment for protein structure homology modelling. *Bioinformatics* 22: 195–201.
43. Zhang Y (2009) I-TASSER: fully automated protein structure prediction in CASP8. *Proteins* 77 Suppl 9: 100–113.
44. Laskowski RA (2001) PDBsum: summaries and analyses of PDB structures. *Nucleic Acids Res* 29: 221–222.
45. Laskowski RA, Watson JD, Thornton JM (2005) ProFunc: a server for predicting protein function from 3D structure. *Nucleic Acids Res* 33: W89–93.
46. Guerler A, Knapp EW (2008) Novel protein folds and their nonsequential structural analogs. *Protein Sci* 17: 1374–1382.
47. Sigrist CJA, Cerutti L, de Castro E, Langendijk-Genevaux PS, Bulliard V, et al. (2010) PROSITE, a protein domain database for functional characterization and annotation. *Nucleic Acids Res* 38: D161–166.
48. Letunic I, Doerks T, Bork P (2009) SMART 6: recent updates and new developments. *Nucleic Acids Res* 37: D229–232.
49. Tusnady GE, Simon I (2001) The HMMTOP transmembrane topology prediction server. *Bioinformatics* 17: 849–850.
50. Krogh A, Larsson B, von Heijne G, Sonnhammer EL (2001) Predicting transmembrane protein topology with a hidden Markov model: application to complete genomes. *J Mol Biol* 305: 567–580.
51. Emanuelsson O, Brunak S, von Heijne G, Nielsen H (2007) Locating proteins in the cell using TargetP, SignalP and related tools. *Nat Protoc* 2: 953–971.
52. Larkin MA, Blackshields G, Brown NP, Chenna R, McGettigan PA, et al. (2007) Clustal W and Clustal X version 2.0. *Bioinformatics* 23: 2947–2948.
53. Comeau SR, Kozakov D, Brenke R, Shen Y, Beglov D, et al. (2007) ClusPro: performance in CAPRI rounds 6–11 and the new server. *Proteins* 69: 781–785.
54. DeLano WL The PyMOL Molecular Graphics System.